Superconductor
Science and
Technology

PURPOSE-LED
PUBLISHING™

PAPER • **OPEN ACCESS**

Coherent control of an exfoliated $NbSe_2$ homojunction qubit in a three-dimensional cavity

To cite this article: A D'Elia *et al* 2026 *Supercond. Sci. Technol.* **39** 115004

View the article online for updates and enhancements.

You may also like

- Design and statistical validation of low-cost electrogoniometers for elbow orthosis applications
José F Escobedo-Magallán, Adriana del Carmen Téllez-Anguiano, Manuel Áviles-Jr et al.
- Dopant-induced modifications of the optical properties of GaSe
Jakub Sójka, Katarzyna Olkowska-Pucko, Kacper Walczyk et al.
- Crack-driven electrical response in stretchable electronics: an original multi-scale characterization
Marie Goizet, Raphaël Passas, Guillaume Krosnicki et al.

This content was downloaded from IP address 87.5.113.34 on 15/11/2026 at 17:17

Superconductor Science and Technology

Check for updates

OPEN ACCESS

RECEIVED
9 June 2026

REVISED
16 October 2026

ACCEPTED FOR PUBLICATION
26 October 2026

PUBLISHED
9 November 2026

Original content from this work may be used under the terms of the Creative Commons Attribution 4.0 licence.

Any further distribution of this work must maintain attribution to the author(s) and the title of the work, journal citation and DOI.



PAPER

Coherent control of an exfoliated $NbSe_2$ homojunction qubit in a three-dimensional cavity

A D'Elia[1,*], F Chiarello[1,2], D Di Gioacchino[1], A S Piedjou Komnang[1], A Giachero[3,4,5], C Ligi[1], G Maccarrone[1], F Mattioli[1,2], C Pira[6], A Rettaroli[1], J Rezvani[1,7], S Tocci[1] and C Gatti[1]

[1] Istituto Nazionale di Fisica Nucleare (INFN), Laboratori Nazionali di Frascati, via Enrico Fermi 54, 00044 Frascati (RM), Italy
[2] Istituto di Fotonica e Nanotecnologie, Consiglio Nazionale delle Ricerche (CNR), 00156 Roma, Italy
[3] Dipartimento di Fisica, Universitá di Milano-Bicocca, Piazza Della Scienza, 3, 20126 Milano, Italy
[4] INFN Milano Bicocca, Piazza Della Scienza, 3, 20126 Milano, Italy
[5] Bicocca Quantum Technologies (BiQuTe) Centre, Piazza Della Scienza, 3, 20126 Milano, Italy
[6] INFN, Laboratori Nazionali di Legnaro, Legnaro, Padova, Italy
[7] Sezione di Fisica, scuola di scienze e tecnologie, Universitá di Camerino, Camerino, Italy
[*] Author to whom any correspondence should be addressed.

E-mail: alessandro.delia@lnf.infn.it

Keywords: NbSe2, qubit, axion, 2D superconductor, Van der Waals qubits

Abstract

Functionalizing quantum devices to extend their range of applications is an extremely active area of research. One of the most promising approaches is to replace aluminum with functional materials. Within this context, van der Waals (vdW) superconductors are ideal candidates because they could enable the integration of their unique properties into qubits. In this work, we present a qubit whose Josephson junction is fabricated from exfoliated $NbSe_2$ using a lithography-free process. Our device exhibits a relaxation time $T_1 = 275 \pm 7$ ns as well as coherence times $T_2^* = 136 \pm 31$ ns and $T_2^{\mathrm{Echo}} = 203 \pm 16$ ns. Our work demonstrates the feasibility of integrating vdW superconductors into quantum technologies and represents a first step toward applying quantum non-demolition photon-detection protocols to the challenging field of dark matter searches.

1. Introduction

Quantum technologies promise to enable applications such as quantum computing, secure data transmission, and detectors sensitive to single energy quanta. One of the fundamental building blocks of quantum technologies are qubits [1, 2], with superconducting qubits representing one of the leading platforms. These devices can be described as nonlinear LC circuits, in which Josephson junctions (JJs) act as nonlinear inductive elements, enabling the realization of quantum two-level systems that can be coherently manipulated using microwave pulses [3]. Standard JJs are typically fabricated in aluminum, a platform supported by a mature fabrication technology that has enabled transmons with coherence times reaching the millisecond scale [4]. Nevertheless, this approach presents certain limitations, including relatively large on-chip footprints and limited compatibility with magnetic environments and topological materials that could enable novel mechanisms of noise protection, such as topologically protected devices [5].

To address these challenges, van der Waals (vdW) materials have emerged as promising candidates for next-generation superconducting circuits. Their layered structure enables the integration of superconductivity with semiconducting, magnetic, and topological two-dimensional systems within a single vertical heterostructure, thereby expanding the functional landscape of superconducting quantum technologies beyond what is achievable with conventional aluminum-based platforms.

The incorporation of vdW materials into quantum technologies has the potential to broaden their scope of applicability [6, 7]. This integration process is already underway and has led to the realization of distinctive devices, including graphene-based gatemons [8], infrared single-photon detectors [9–12], $NbSe_2$-graphene hybrid superconducting quantum interference devices [13], and superconducting

© 2026 The Author(s). Published by IOP Publishing Ltd

diodes [14, 15]. Moreover, both qubit density per chip [16, 17] and the development of novel qubit architectures [18] could benefit from vdW-based quantum devices.

The push to realize novel vdW quantum devices with new functional properties finds a natural outcome in the demanding field of dark matter searches, where the use of quantum devices is quickly becoming a standard approach [19]. For example, the extreme sensitivity required for dark-photon or axion searches can only be matched by quantum non-demolition photon-detection schemes based on qubit-photon entanglement [20, 21]. Axion searches pose an additional challenge because the intense magnetic field required for axion-to-photon conversion would disrupt superconductivity in the qubit, making aluminum-based technology unsuitable for this task. A magnetic-field-resistant qubit would enable quantum non-demolition schemes as well as searches through direct qubit excitation [22]. In this context, $NbSe_2$ emerges as a natural candidate for the realization of magnetic-field-resistant quantum devices because it can withstand fields up to 30 T [23]. While the $NbSe_2$ nonlinear element is therefore promising for high-field operation, the present implementation still relies on an Al cavity and Al shunting electrodes, which are not suitable for the multi-tesla fields required in axion haloscopes. The present work should thus be regarded as a proof of principle of the $NbSe_2$-based nonlinear element, while a future high-field-compatible architecture will require replacing the Al components and directly characterizing the device under a magnetic field. Although this technology is still in its infancy, recent demonstrations of coherent $NbSe_2$-based qubits mark a crucial first step toward establishing $NbSe_2$ as a viable platform for superconducting quantum devices [24]. In this work, we present the characterization of a $NbSe_2$-based qubit that exhibits coherent oscillations with a relaxation time $T_1 = 275 \pm 7$ ns as well as coherence times $T_2^* = 136 \pm 31$ ns and $T_2^{\mathrm{Echo}} = 203 \pm 16$ ns. To our knowledge, these devices represent the first demonstration of coherent $NbSe_2$-based qubits integrated into a three-dimensional cavity. Our results highlight the potential of integrating vdW superconductors into quantum devices and constitute a first step toward demanding applications such as quantum non-demolition single-photon detection in the presence of magnetic fields.

2. Experimental

The devices consist of a $NbSe_2$–$NbSe_2$ homojunction (HQ Graphene) [25] embedded inside an Al rectangular cavity. To fabricate the JJ, we used polymer-based dry transfer techniques [26]. We assembled the homojunction at INFN Laboratori Nazionali di Frascati using two successive pickup steps. In the first step, the bottom flake was selected and transferred onto the Al electrodes. The same procedure was then applied to position the top flake, resulting in an overlap area of 13 μm^2. The entire fabrication process was carried out in air, and no post-fabrication cleaning steps were performed to remove surface contaminants. This procedure allowed the formation of native NbO_x that acts as a tunnel barrier between the two flakes. Since the $NbSe_2$ flakes are transferred onto pre-patterned Al electrodes exposed to ambient conditions, a finite Josephson coupling across the Al–$NbSe_2$ interfaces cannot, in principle, be excluded. Although our experimental observations indicate that these interfaces do not provide a significant contribution to the observed nonlinearity, their possible role and the supporting experimental evidence are discussed in detail in appendix B. Using atomic force microscopy (AFM), we measured the flake thicknesses to be 20 nm (bottom) and 13 nm (top) (see appendix D). The JJ was shunted by two circular Al pads of diameter 1000 μm and separated by 1483 μm (details on the e-beam lithography process can be found in appendix 1(a). An optical image of the $NbSe_2$ JJ is shown in figure 1(a), and the radio-frequency (RF) measurement setup is shown in figure 1(b). The aluminum cavity, of purity 99.999% and dimensions $L_x \times L_y \times L_z = 26 \times 36 \times 8$ mm^2, was produced at INFN Laboratori Nazionali di Legnaro (see appendix A for additional details).

The device was measured at a temperature of ∼20 mK in the dilution refrigerator of the Cryogenic Laboratory for Detectors at the Laboratori Nazionali di Frascati of INFN. The measurement setup is shown in figure 1(b). The dashed black lines and boxes indicate the different temperature stages of the cryostat. Line 1 refers to the attenuated input RF transmission line, whereas Line 5 refers to the low-loss, amplified output line. The aluminum cavity was protected with infrared filters, while an isolator shielded the output from backward-propagating radiation from the high-electron-mobility transistor (HEMT) amplifier at 4 K. The RF signals for readout and control of the qubit were generated on two independent channels of the Keysight quantum control system (QCS). The QCS was also used to collect the output signal.

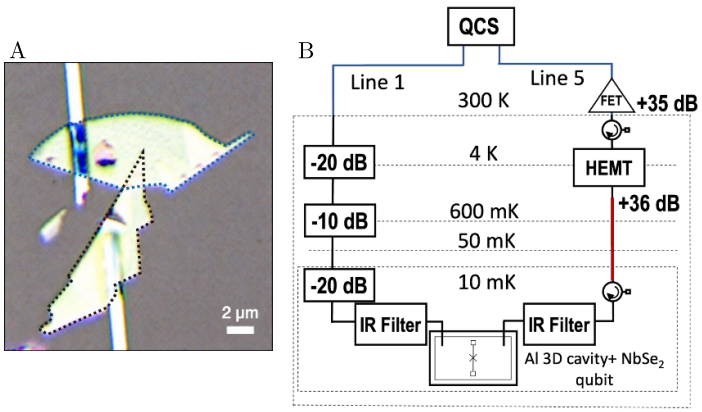


Figure 1. (A) Optical image of the JJ. The overlap area between the two flakes is 13 μm^2. (B) RF schematic of the $NbSe_2$ qubit measurement setup. The components inside the dashed box are located inside the cryostat at different temperature stages. The lines highlighted in red represent superconducting cables.

3. Results

We first characterized the coupled qubit-resonator system through resonator and two-tone spectroscopy. The system can be described within the dispersive regime of the Jaynes–Cummings model. Setting $\hbar = 1$, the effective Hamiltonian reads

$$H_{\mathrm{JC}} = \left(\omega_{\mathrm{r}} - \frac{\chi_{12}}{2} + \chi\sigma_z\right) a^{\dagger}a + \frac{1}{2}\left(\omega_{\mathrm{q}} + \chi_{01}\right)\sigma_z \tag{1}$$

where ω_{r} and ω_{q} are the bare resonator and qubit frequencies, respectively, $a^{\dagger}$ (a) is the photon creation (annihilation) operator of the resonator mode, and σ_z is the Pauli-z operator acting on the qubit subspace. The quantities χ_{01} and χ_{12} are the dispersive shifts associated with the $|0\rangle \leftrightarrow |1\rangle$ and $|1\rangle \leftrightarrow |2\rangle$ transitions, respectively,

$$\chi_{ij} = \frac{g_{ij}^2}{\Delta_{ij}}, \qquad \Delta_{ij} = \omega_{ij} - \omega_{\mathrm{r}}, \tag{2}$$

where g_{ij} is the corresponding qubit-resonator coupling strength and Δ_{ij} is the detuning from the resonator. The total dispersive shift is

$$\chi = \chi_{01} - \frac{\chi_{12}}{2}. \tag{3}$$

We initially performed resonator spectroscopy of the transverse electric (TE) TE_{110} mode, as shown in figure 2(a). At high readout power, the qubit-resonator interaction becomes effectively saturated and the bare resonator frequency emerges at $\omega_{\mathrm{r}}/2\pi = f_{\mathrm{r}} = 7.28551$ GHz. From the measured resonator frequency shift, we estimate $\chi_{01}/2\pi = 142$ kHz.

We then performed two-tone spectroscopy to determine the transmon transition frequencies. As shown in figure 2(b), the fundamental transition is observed at $\omega_q/2\pi = f_{01} = 10.778$ GHz, while the two-photon $|0\rangle \leftrightarrow |2\rangle$ transition occurs at $f_{02}/2 = 10.535$ GHz. This gives

$$f_{12} = f_{02} - f_{01} = 10.292 \text{ GHz}, \tag{4}$$

and an anharmonicity

$$\alpha = f_{01} - f_{12} = 486 \text{ MHz}. \tag{5}$$

Combining the measured χ_{01} with the qubit-resonator detuning, $\Delta_{01}/2\pi = f_{01} - f_{\mathrm{r}} = 3.49249$ GHz, we extract a coupling strength of

$$g_{01}^{110}/2\pi = 22.2 \text{ MHz}. \tag{6}$$

Finally, using the transmon relation $g_{12} \simeq \sqrt{2}g_{01}$ together with the measured f_{12}, we estimate $\chi_{12}/2\pi \simeq 328$ kHz. The resulting total dispersive shift is therefore

$$\chi/2\pi = \chi_{01}/2\pi - \chi_{12}/4\pi \simeq -22 \text{ kHz}. \tag{7}$$

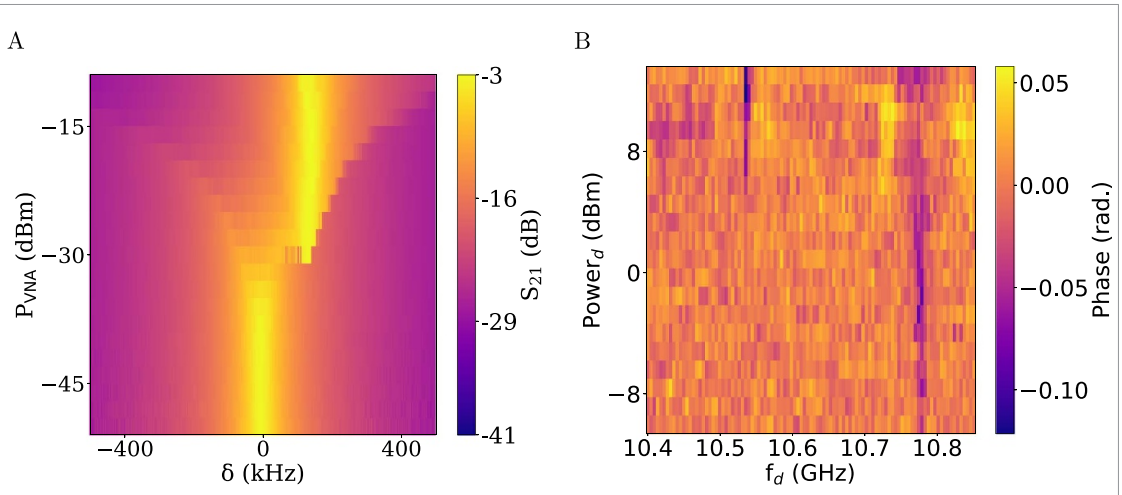


Figure 2. (A) Resonator spectroscopy for the 110 mode. (B) Qubit spectroscopy. The drive power is expressed as the generator output power. The appearance of the $f_{02}/2$ absorption peak can be clearly observed for $P_d \simeq 6$ dBm.

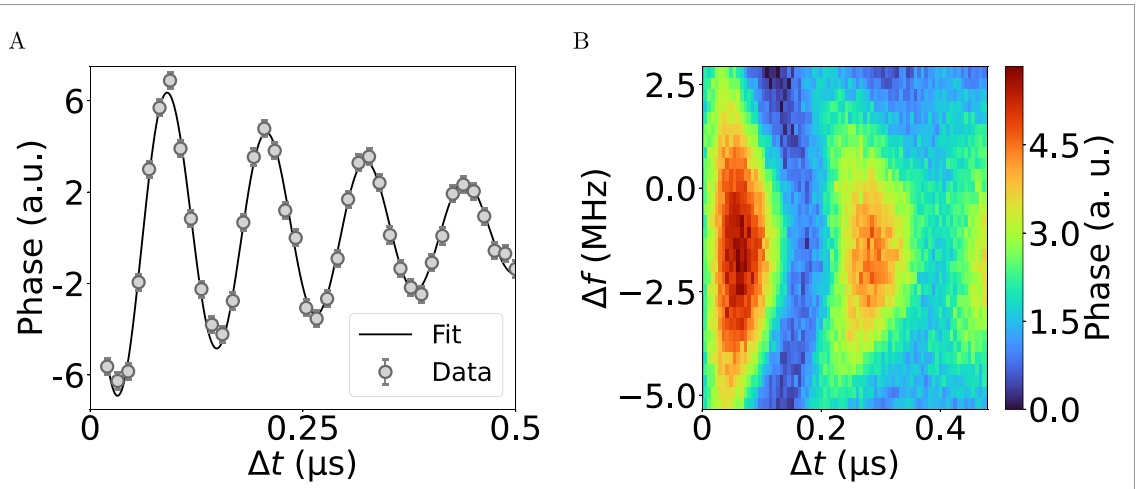


Figure 3. (A) Rabi oscillations for $f_d = f_{01}$ and drive power $P_d = 0$ dBm (generator output power). (B) Chevron plot of the $NbSe_2$ qubit. $P_d = -4.5$ dBm.

We continued the characterization of the qubit in the time domain. We performed Rabi spectroscopy by applying excitation pulses of varying duration, Δt, at the transition frequency f_{01} while monitoring the phase of the transmitted signal. The resulting Rabi oscillations confirm the coherent control of the device as shown in figure 3. We then measured the Rabi frequency as a function of the drive amplitude, expressed in terms of the square root of the effective cavity occupation number $\sqrt{n_\gamma}$. The observed linear dependence, discussed in appendix H, indicates that the qubit dynamics remains predominantly confined to the $|0\rangle$–$|1\rangle$ subspace, consistent with the large anharmonicity observed [27–29]. Finally, we measured the dependence of the qubit response on the excitation detuning and pulse duration through a Chevron experiment. The resulting Chevron plot, shown in figure 3(b), was used to calibrate the excitation frequency and the duration of the π pulse.

We measured the relaxation time T_1 and the decoherence times T_2^* and T_2^{Echo} (see figure 4). Fits to the globally averaged traces yield $T_1 = 275 \pm 7$ ns, $T_2^* = 136 \pm 31$ ns, and $T_2^{\text{Echo}} = 203 \pm 16$ ns.

To assess the variability of the coherence properties across repeated acquisitions, we performed multiple independent time-domain measurements and analyzed the distributions of the individually fitted decay times. The 48 independent T_1 measurements yield a mean of 280 ± 10 ns, a median of 270 ns, and a standard deviation of 72 ns. The T_2^* distribution, obtained from 21 measurements, has a mean of 130 ± 20 ns, a median of 112 ns, and a standard deviation of 81 ns. Finally, the 44 independent T_2^{Echo} measurements yield a mean of 300 ± 30 ns, a median of 247 ns, and a standard deviation of 185 ns. The uncertainties on the distribution means are calculated as standard deviation divided by the square root of the number of individual measurements ($s/\sqrt{N}$), rounded to one significant digit; the means are

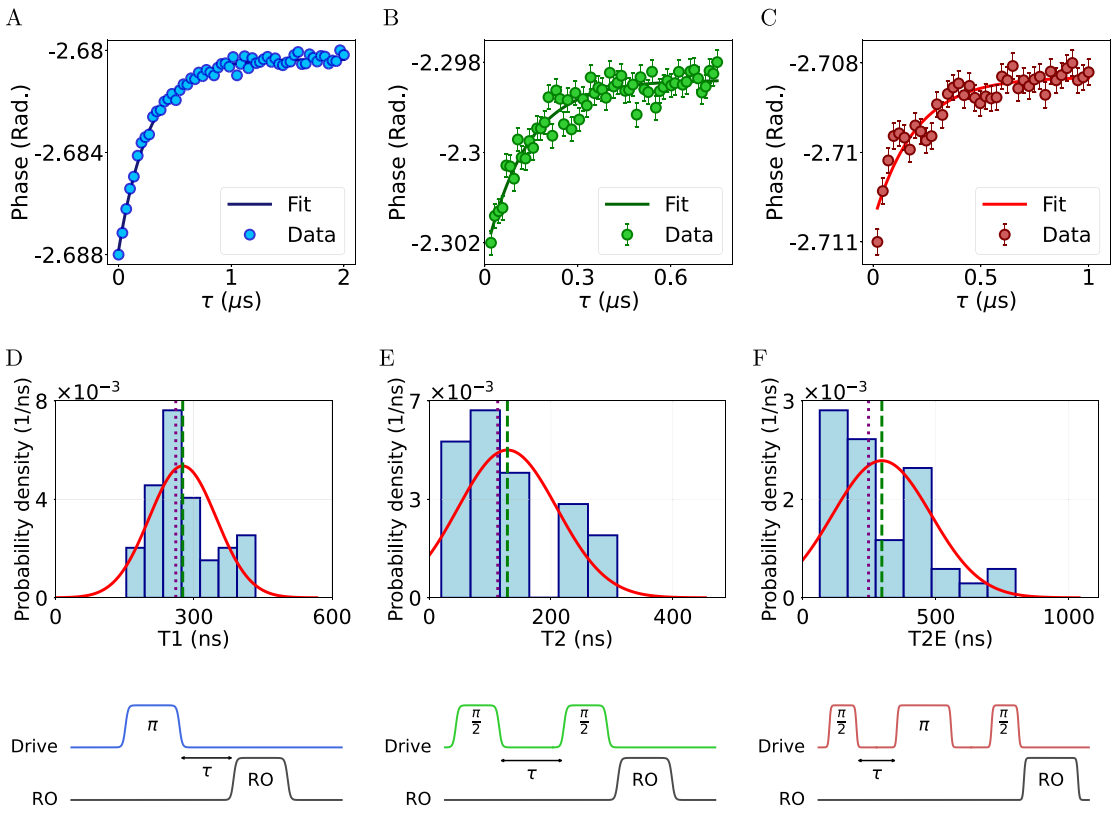


Figure 4. Fits to the globally averaged T_1 (A), T_2^* (B), and T_2^{Echo} (C) measurements. (D)–(F) Distributions of the measured coherence times T_1, T_2^*, and T_2^{Echo}, respectively. The T_1 distribution, obtained from 48 independent measurements, has a mean of 280 ± 10 ns, a median of 270 ns, and a standard deviation of 72 ns. The T_2^* distribution, obtained from 21 independent measurements, has a mean of 130 ± 20 ns, a median of 112 ns, and a standard deviation of 81 ns. The T_2^{Echo} distribution, obtained from 44 independent measurements, has a mean of 300 ± 30 ns, a median of 247 ns, and a standard deviation of 185 ns. Uncertainties on the means are standard errors, calculated as $s/\sqrt{N}$, where s is the sample standard deviation and N is the number of independent measurements. Solid lines in (D)–(F) represent Gaussian fits to the corresponding distributions, the purple (dotted) lines represent the median and the green (broken) lines represent the mean. The pulse sequences used for the T_1, T_2^*, and T_2^{Echo} measurements are shown at the bottom. RO denotes the readout pulse. For these measurements $t_\pi = 150$ ns, $t_{\pi/2} = 75$ ns.

rounded to the same decimal place. These uncertainties are distinct from those of the fits to the globally averaged traces.

The decay times extracted from the globally averaged traces do not necessarily coincide with the means of the individually fitted values. The global $T_1 = 275$ ns is consistent with the distribution mean of 280 ± 10 ns, while the global $T_2^* = 136$ ns is close to its mean of 130 ± 20 ns. In contrast, the global $T_2^{\text{Echo}} = 203$ ns lies below both the mean and the median of the individual measurements. This discrepancy is not intrinsically inconsistent: averaging decay traces and subsequently fitting them is not equivalent to averaging the decay times obtained from separate fits. Even when individual traces follow a single-exponential decay, their average generally does not, and the effective decay time extracted from it depends on the distribution of decay times, the relative signal amplitudes, and the fitting procedure.

The echo measurements show the largest absolute spread, and their mean exceeds their median, consistent with an asymmetric distribution extending toward longer decay times. Such longer-lived acquisitions can raise the arithmetic mean without producing a comparable increase in the decay time extracted from the averaged trace. However, the summary statistics alone do not establish the origin of the observed discrepancy. The spread of the fitted values may reflect both acquisition-to-acquisition variability and uncertainty in the individual fits. Nevertheless, both the global fits and the distribution central values give longer coherence times for the echo sequence than for Ramsey measurements, consistent with partial refocusing of slow dephasing fluctuations. We believe the time-domain performance is currently limited by uncontrolled parameters in the fabrication process, such as high-density clusters of $NbSe_2$ flakes near the JJ that offer additional dissipation channels, as well as bubbles or organic polymer residues on the JJ caused by the dry-transfer process. These factors can be minimized by post-fabrication annealing and mechanical removal of excess flakes [30] and should not affect next-generation devices.

Nevertheless, our results show that dry transfer exfoliation is a valid method to fabricate $NbSe_2$ qubits. These findings are a first step in progressing toward the realization of magnetic-field-resistant qubits for dark matter searches.

4. Conclusions

We demonstrated the fabrication and coherent control of an $NbSe_2$ homojunction qubit using dry exfoliation and transfer of individual $NbSe_2$ flakes. The device exhibits an anharmonicity of 486 MHz, a relaxation time of $T_1 = 275 \pm 7$ ns, and coherence times of $T_2^* = 136 \pm 31$ ns and $T_2^{\mathrm{Echo}} = 203 \pm 16$ ns. The observed Rabi oscillations and large anharmonicity are consistent with coherent dynamics predominantly within the computational subspace $|0\rangle$-$|1\rangle$. To our knowledge, this is the first demonstration of coherent control of an exfoliated $NbSe_2$ homojunction qubit integrated into a three-dimensional cavity. These results establish dry-transfer assembly as a viable route for integrating vdW superconductors into superconducting quantum circuits. The integration of vdW superconductors offers opportunities to develop quantum devices with properties and functionalities beyond those available in conventional platforms. In particular, $NbSe_2$-based qubits provide a promising direction toward quantum-enhanced axion detection, through both direct qubit excitation within axion cavities [22] and quantum non-demolition photon-detection protocols. Realizing these applications will require a fully magnetic-field-compatible architecture, including replacement of the aluminum cavity and electrodes used here, and direct characterization under an applied magnetic field. Mechanical exfoliation and dry transfer provide a flexible fabrication approach for exploring such devices, particularly in applications requiring a limited number of qubits. This work therefore represents a step toward vdW-based quantum circuits for precision sensing and fundamental physics experiments.

Acknowledgments

This work was supported by RESILIENCE, Qub-IT and QUART&T, Projects funded by INFN within the Technological and Interdisciplinary Research Commission, and by Projects funded under the Piano Nazionale di Ripresa e Resilienza (PNRR) by the Ministero dell'Universitá e della Ricerca (MUR): PE0000023-NQSTI and CN00000013-ICSC. We thank Massimo Bauco (Rohde & Schwarz Roma) for support with reverse sweeps of the vector network analyzer (VNA), and Marco Beatrici for technical support in the laboratory.

Data availability statement

The data cannot be made publicly available upon publication because no suitable repository exists for hosting data in this field of study. The data that support the findings of this study are available upon reasonable request from the authors.

Author contributions

A D'Elia 0000-0002-6856-7703
Data curation (equal), Formal analysis (equal), Funding acquisition (equal), Investigation (lead), Methodology (equal), Resources (equal), Validation (lead), Writing – original draft (equal), Writing – review & editing (equal)

F Chiarello 0000-0002-7487-2827
Formal analysis (equal), Writing – review & editing (equal)

D Di Gioacchino 0000-0002-1288-4742
Methodology (equal)

A S Piedjou Komnang 0000-0003-2430-0086
Formal analysis (equal)

A Giachero 0000-0003-0493-695X
Funding acquisition (equal), Resources (equal)

C Ligi 0000-0001-7943-7704
Methodology (equal)

G Maccarrone 0000-0002-7234-9522
Methodology (equal)

F Mattioli 0000-0002-7242-3366
Investigation (equal), Resources (equal)

C Pira 0000-0002-5893-1567
Methodology (equal)

A Rettaroli 0000-0001-6080-8843
Investigation (equal), Methodology (equal)

J Rezvani 0000-0002-6771-170X
Investigation (equal), Writing – review & editing (equal)

S Tocci 0000-0002-5800-5408
Investigation (equal), Methodology (equal)

C Gatti 0000-0003-3676-1787
Data curation (equal), Formal analysis (equal), Funding acquisition (equal), Methodology (equal), Resources (equal), Writing – original draft (equal), Writing – review & editing (equal)

Appendix A. Cavity and pre-patterned chip fabrication

To reduce the cavity surface roughness after mechanical machining, two treatments were performed: a 24 h tumbling treatment with coco powders followed by 1 h of electropolishing in a 65:35 solution of phosphoric acid and butyl acetate at 60 °C. The two processes removed about 20–30 μm of Al from the surface. The pre-patterned substrate was fabricated at the Istituto di Fotonica e Nanotecnologie of CNR using electron-beam lithography (EBL) and lift-off techniques. To enhance the lift-off quality, a bilayer resist structure was used. It was made of a first layer of poly(methyl methacrylate-co-methacrylic acid) (AR-P 617.08), followed by a 6% poly(methyl methacrylate) (PMMA; AR-P 669.06) layer. The bilayer was covered with an anti-charging film (AR-PC 5090). A Raith Voyager 50 kV EBL system was used to expose the pattern made for the two circular Al pads (1000 μm in diameter) and two wires, each 2 μm wide, that connect them to the central area where the junction was then fabricated. After development in a 1:3 mixture of methyl isobutyl ketone and isopropyl alcohol, 80 nm of aluminum was deposited by electron-beam evaporation, followed by lift-off using hot acetone. The full device assembly (cavity and qubit) is shown in figure 5.



Figure 5. Aluminum cavity containing the qubit.

Appendix B. Possible Josephson coupling at the Al-$NbSe_2$ interfaces

An additional consideration in the interpretation of the device concerns the electrical contacts between the $NbSe_2$ flakes and the pre-patterned Al electrodes. The Al electrodes were exposed to air for several hours before the $NbSe_2$ transfer, which was subsequently performed under ambient conditions. No *in situ* cleaning or oxide-removal procedure was performed prior to establishing the Al-$NbSe_2$ contacts. Therefore, the presence of a native AlO_x layer and surface adsorbates at these interfaces is expected. In principle, an Al/AlO_x/$NbSe_2$ interface could support a finite Josephson coupling. If both Al-$NbSe_2$ contacts behaved as Josephson weak links, the device would contain three nonlinear elements rather than a single $NbSe_2$/$NbSe_2$ junction. We stress, however, that these interfaces were neither intentionally fabricated nor independently characterized as JJs. Their presence alone is therefore insufficient to establish a measurable Josephson coupling or its magnitude.

If a finite Josephson coupling were present at the Al-$NbSe_2$ interfaces, the circuit Hamiltonian would contain multiple Josephson contributions. Denoting the phase drops across the three interfaces by φ_i, the nonlinear potential would take the general form

$$U_J = -\sum_i E_{J,i} \cos \varphi_i \,,$$

with $E_{J,i}$ the corresponding Josephson energies. In the limit in which the intermediate nodes do not constitute independent dynamical degrees of freedom, the circuit can still be described by a single collective mode. The total phase drop is then distributed among the nonlinear elements according to their inductive participation. At the quadratic level, their Josephson inductances contribute in series, whereas the nonlinear contribution of each element is weighted by its phase participation. Additional weak links in series would therefore generally redistribute the phase and dilute the anharmonicity associated with the dominant junction.

A different regime would arise if the capacitances associated with the intermediate nodes were sufficiently large to introduce additional dynamical degrees of freedom. The circuit would then require a multi-mode description based on the full capacitance matrix and multiple phase coordinates. In this case, the spectroscopically observed transition and the measured relaxation and coherence times would correspond to a collective normal mode of the complete circuit rather than to an isolated $NbSe_2$/$NbSe_2$ junction.

For the present devices, the critical currents of the possible Al/AlO_x/$NbSe_2$ weak links cannot be independently determined. Consequently, their phase participation cannot be quantitatively extracted and a multi-junction Hamiltonian cannot be constrained from the available measurements. Nevertheless, our experimental observations suggest that any Josephson coupling associated with these interfaces has a small participation in the measured qubit mode.

First, the device displays a well-resolved qubit transition with a large anharmonicity and coherent two-level dynamics, including a clear Rabi chevron and well-defined T_1, T_2, and $T_{2,\mathrm{echo}}$ measurements. No additional spectroscopic transitions attributable to extra junction degrees of freedom are resolved within the investigated frequency and power ranges. While this observation does not exclude additional weak links, it is consistent with the $NbSe_2$/$NbSe_2$ junction providing the dominant nonlinear contribution to the observed mode.

Additional information is provided by the high-temperature/high-photon-population resonator measurements reported in figure 13 of appendix E. Under these conditions, no additional instability or transition attributable to the Al-$NbSe_2$ contacts was observed. If these interfaces behaved as Josephson weak links with appreciable phase participation, their response to increased thermal and microwave excitation could in principle produce additional nonlinear features. Their absence provides further, although indirect, evidence that the measured nonlinearity is not dominated by the Al-$NbSe_2$ interfaces.

Finally, we fabricated an additional structure in which a single $NbSe_2$ flake directly bridges the two Al electrodes, thereby removing the $NbSe_2$/$NbSe_2$ junction while retaining two Al-$NbSe_2$ interfaces fabricated using the same procedure. No nonlinear response was observed in this device, including at high readout powers. This control experiment does not constitute a definitive demonstration of vanishing Josephson coupling at an individual Al-$NbSe_2$ interface, since the microscopic properties of the contacts may vary between devices. However, it provides direct experimental evidence that Al-$NbSe_2$ contacts produced with our fabrication process do not, by themselves, generate a detectable Josephson nonlinearity under the measurement conditions explored here.

Taken together, these observations support our interpretation that the $NbSe_2$/$NbSe_2$ junction is the dominant nonlinear element responsible for the observed qubit behavior. A weak residual Josephson

coupling across the Al-$NbSe_2$ interfaces cannot be excluded, and its precise contribution would require dedicated test structures and independent characterization of the interface critical currents. Within the resolution of the present measurements, however, we find no experimental evidence that these interfaces contribute appreciably to the nonlinear dynamics of the device.

Appendix C. Additional devices

To substantiate the results obtained with the first device, we fabricated three additional devices using the same procedures described in this manuscript, with the only difference being that the chip substrate was silicon instead of sapphire for device Q1. The pad geometry is identical to that used in the main text, consisting of two circular pads with a diameter of 1000 μm. Of the three devices, two exhibited clear nonlinear behavior during RF characterization, while the third was short-circuited due to a fabrication error. The overall fabrication yield is therefore 75% over four devices. For device Q2, the experimental setup is identical to that described in the main text; for device Q1, it is shown in figure 6.

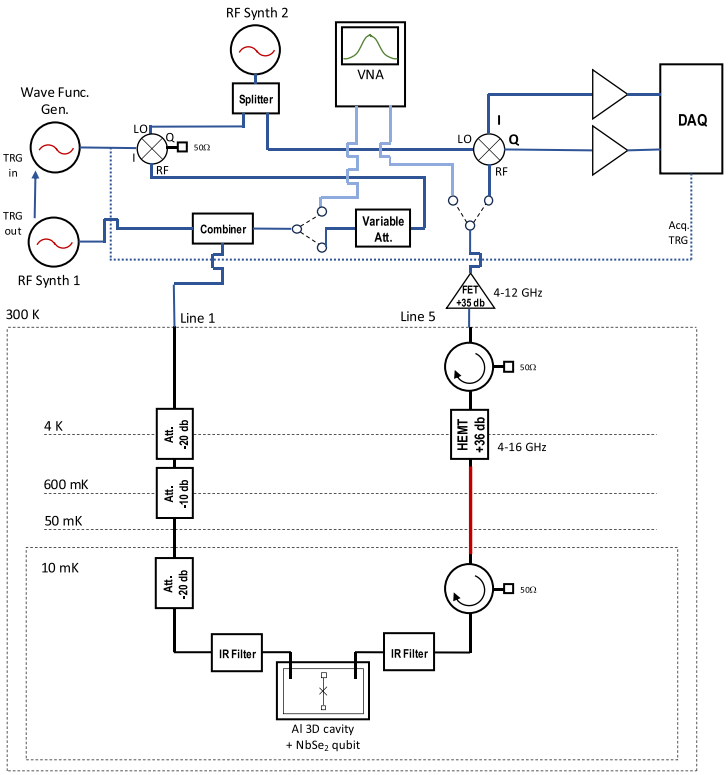


Figure 6. Experimental schematic. The upper part shows the room-temperature instrumentation and wiring; the lower part, enclosed by the dashed black box labeled 300 K, shows the setup in the dilution refrigerator. The red line is a superconducting NbTi cable for low-loss transmission. The in-phase/quadrature (I)–(Q) mixers used as a vector modulator and a down-converter are the same model. The small dashed lines with open circles at their edges represent mechanical switches.

AFM measurements indicate junction areas of 77 μm^2 (device Q1, vq = 12.611 GHz) and 14.2 μm^2 (device Q2, vq = 16.378 GHz), respectively (see appendix D). For device Q1, the observed behavior is that of a device with low anharmonicity that behaves as a Duffing oscillator (see figure 7).

Nevertheless, we measured coherent oscillations and a relaxation time of 6.5 ± 0.4 μs as reported in figure 8.

The anharmonicity of this device was estimated to be approximately 100 kHz. Therefore, we could not ensure that the system remained confined to the $|0\rangle$-$|1\rangle$ subspace during qubit manipulation. At the time these measurements were performed, we did not have access to pulse-shaping techniques, such as derivative removal by adiabatic gate, that could suppress leakage to higher excited states and improve confinement within the computational subspace.

We characterized device Q2 by performing resonator and qubit spectroscopy. Resonator spectroscopy of the transverse magnetic (TM) modes TM110 and TM130 revealed clear nonlinear behavior as a function of the probe power. In the qubit spectroscopy, we observed the f_{01} transition at 16.378 GHz,

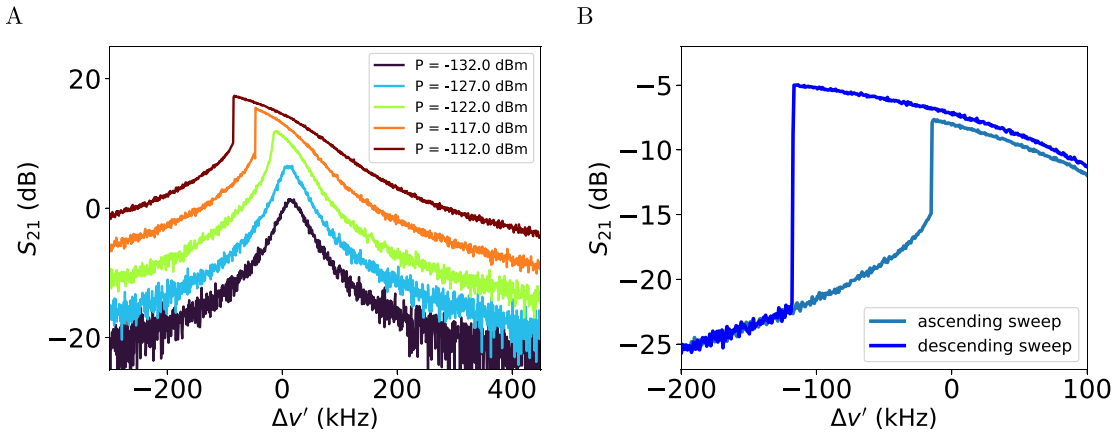


Figure 7. (A) Evolution of the dressed cavity transmission as a function of the readout power (readout frequency expressed relative to $\nu_r = 7.1873$ GHz). The appearance of a step-like resonance indicates that our system behaves as a Duffing oscillator. The spectra are vertically shifted for better visualization. (B) Hysteresis of the Duffing oscillator, depending on whether the frequency is swept from low to high (ascending) or vice versa (descending).

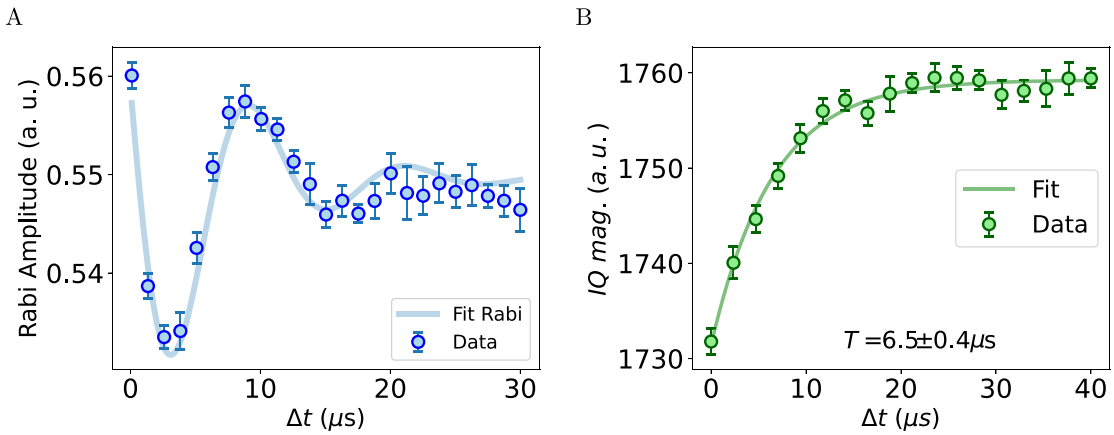


Figure 8. (A) Rabi oscillation of the qubit for a drive power $P = -95$ dBm as a function of the duration of the drive pulse Δt. (B) Decay time T expressed as a function of the delay between the π excitation pulse and the readout, acquired with power $P = -124$ dBm.

together with a weaker peak at 16.358 GHz, which we attribute to the $f_{02}/2$ transition. The resulting anharmonicity is estimated to be approximately 40 MHz (see figure 9). Time-domain measurements were not performed on this device, as it is only weakly coupled to the readout modes within the bandwidth of the amplification chain. The characterization of these additional devices reveals a significant variability in the performance of $NbSe_2$-based qubits. The observed device-to-device variability may arise from several factors, including polymer residues introduced during the exfoliation and dry-transfer process, differences in junction area and substrate, and variations in the properties and microscopic structure of the native oxide barrier. This issues could be mitigated by implementing a post-fabrication in-vacuum annealing step, which would help remove polymer residues while simultaneously minimizing the oxidation of $NbSe_2$ as well as a fabrication protocol for JJ with controlled area.

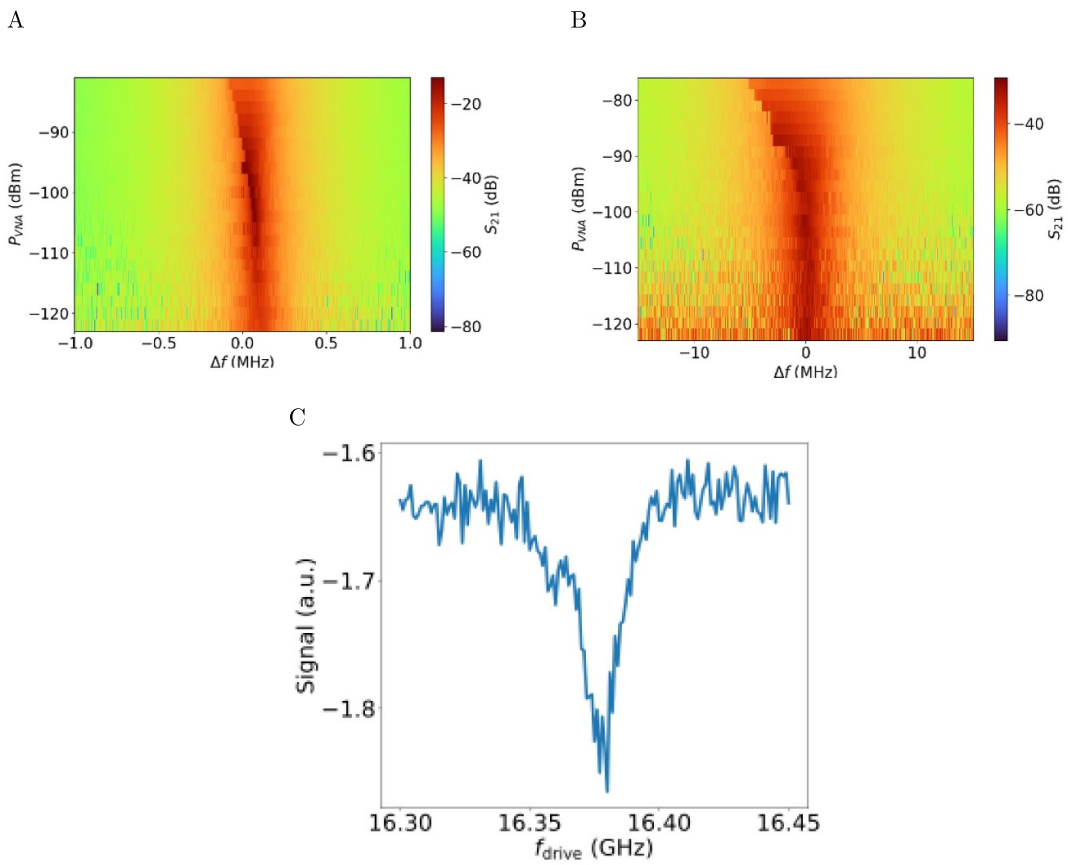


Figure 9. (A) Resonator spectroscopy of the TM110 mode. (B) Resonator spectroscopy of the TM130 mode. (C) Two tones spectroscopy of device Q2.

Appendix D. AFM characterization

We characterized the nanoscale structure of our $NbSe_2$ qubit using AFM. Figure 10 shows a three-dimensional AFM map of the $NbSe_2$ homojunction, in which the overlap region between the two flakes is clearly visible. The overlap area was measured to be approximately 13 μm^2.

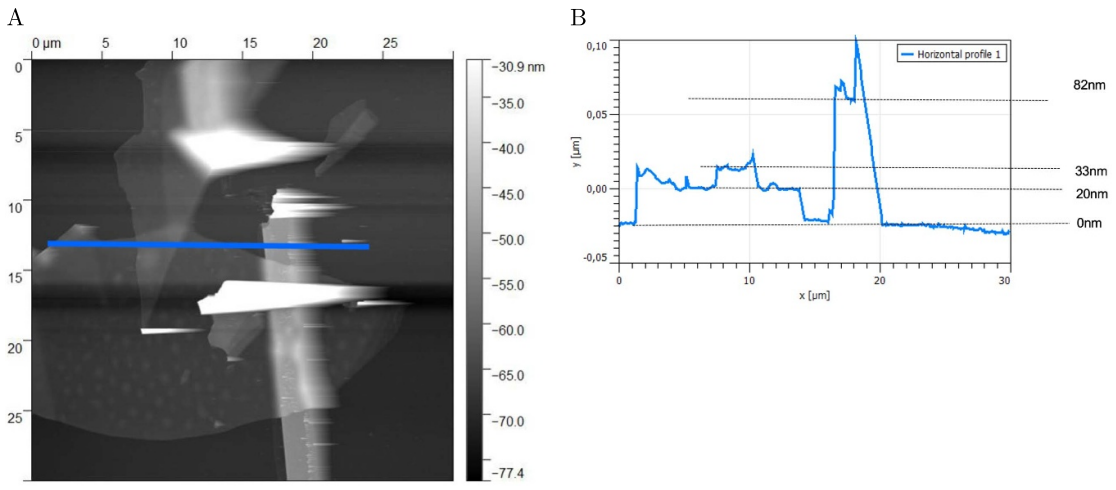


Figure 10. (A) AFM map of the $NbSe_2$ qubit (device Q0). (B) Height profile along the blue line shown in panel A. The bottom flake is 20 nm thick while the top flake is 13 nm thick. The 82 nm structure is the Al wire connection to the circular pads.

The thickness of the individual $NbSe_2$ flakes was determined from the height profile along the line indicated in figure 10(a), with the corresponding line profile shown in figure 10(b). The measured thicknesses are approximately 20 nm for the bottom flake and 13 nm for the top flake.

The AFM map also reveals the presence of residual material and polymer residues on the flake surfaces (white regions in figures 10(a) and 11(b)), likely originating from the fabrication and transfer processes. These observations highlight the need for improved surface-cleaning procedures, including the implementation of a vacuum-baking step, in future generations of devices. Figure 10(b) shows the AFM images of devices Q1 and Q2.

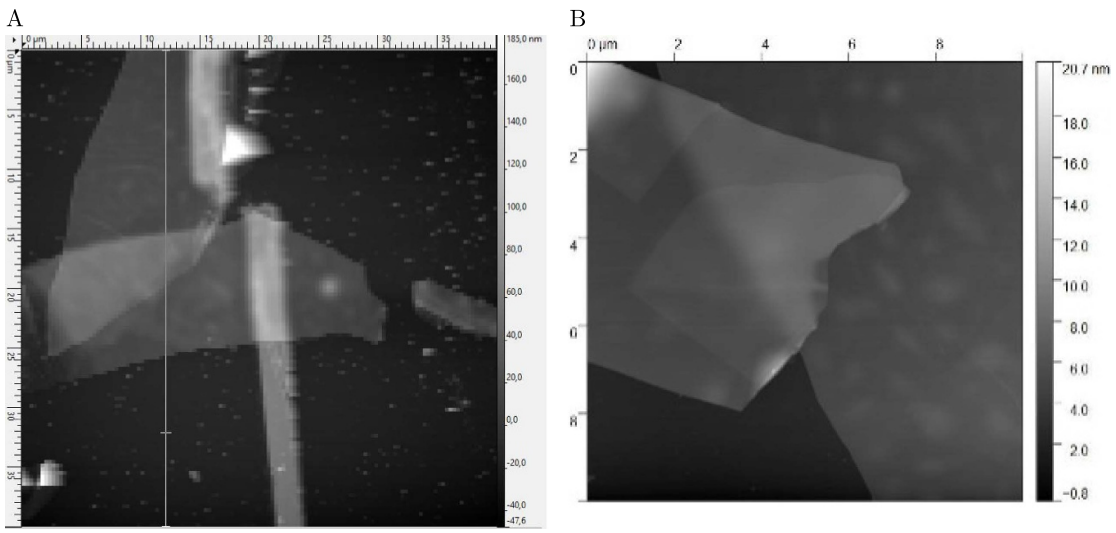


Figure 11. (A) AFM map of device Q1. (B) AFM map of device Q2.

Appendix E. Spectroscopic robustness against thermal noise. Q1

In our experimental setup we had a second qubit, an Al transmon hosted in its Al cavity. This qubit was placed in the cryostat together with the Q1 device and was connected to the same input and output RF-lines (see figure 12(a)). The cavity of the Al qubit was geometrically identical to the $NbSe_2$ one. We performed two different experimental runs, with and without the isolator on the 10 mK stage. This allowed us to verify the thermal noise resistance of the $NbSe_2$ qubit.

In absence of the 10 mK circulator, the devices were not screened by the thermal noise coming from the higher temperature stage of the cryostat, and experienced the emission of a 4 K black-body radiation coming from the HEMT. In this case, we estimated the temperature inside the cavity by assuming that the input and output ports had the same coupling γ to the cavity. The input power, dominated by the 4 K radiation, is $P_{\rm in} = 4k_B\gamma$ while the total power emitted from the two ports is $P_{\rm out} = k_B T_{\rm cav} 2\gamma$, where $T_{\rm cav}$ is the cavity temperature. At thermal equilibrium, and neglecting losses in the cavity and in the coax cables, $P_{\rm in} = P_{\rm out}$ and $T_{\rm cav} \simeq 2$ K, equivalent to $\sim$5 thermal photons on average. We emphasize that this estimate should be regarded only as an order-of-magnitude evaluation based on this simplified thermal model, and not as a calibrated measurement of the intracavity photon occupation. The effect of the thermal noise for the Al device is evident in figures 12(b) and (c) where we compare the distributions of the cavity transmission as a function of power and frequency of the excitation tone in the two experimental configurations. The power for which the bare resonator frequency appears increases from -122 dBm without isolator to –104 dBm with isolator.

In figure 13 we report the resonator spectroscopy measurements for the $NbSe_2$ qubit acquired in the same conditions as those reported in figure 12. The effect of the insulator is minimal confirming the high robustness against thermal noise of device Q1.

The high resistance thermal noise of device Q1 is due to its high critical current I_c. JJs have, in fact, a transition to the normal state when they are crossed by a current larger than I_c. This happens when

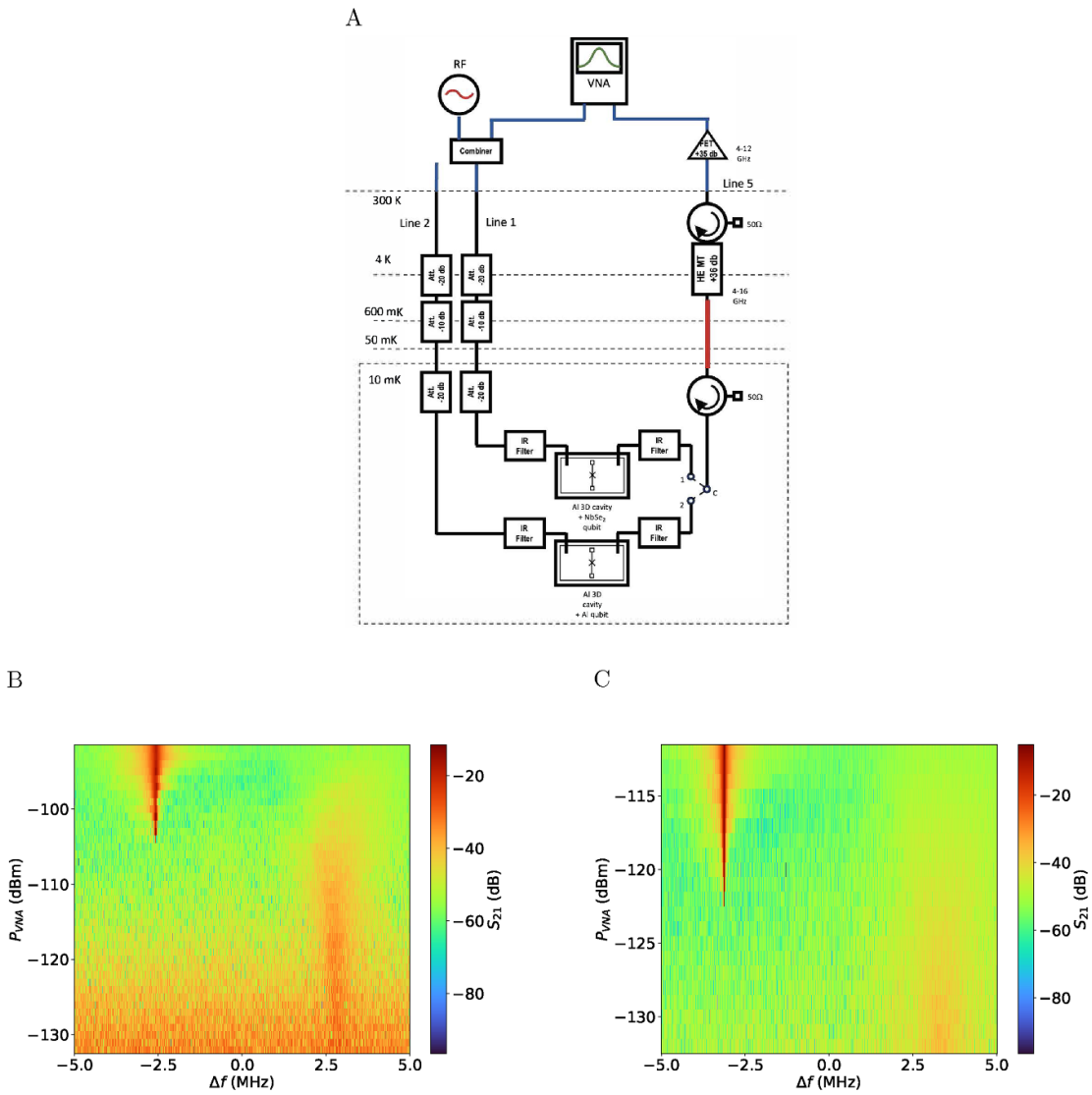


Figure 12. (A) RF scheme of the experimental setup with two cavities and two qubits. Resonator spectroscopy of the Al qubit measured with the 10 mK isolator (B) and without the 10 mK isolator (C). The x axis is expressed as detuning from $f = 7.2553$ GHz.

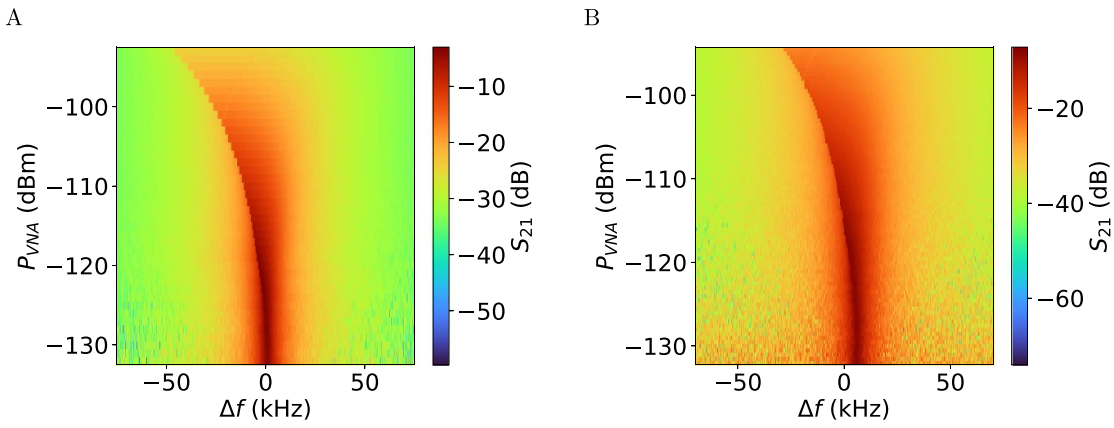


Figure 13. Resonator spectroscopy of the $NbSe_2$ qubit measured with the 10 mK isolator (A) and without the 10 mK isolator (B). The x axis is reported as detuning from $f = 7.1873$ GHz.

the inductive energy $E_L = L_J I_c^2/2 = E_J/2$, where $L_J = \phi_0/(2\pi I_c)$ is the junction inductance, ϕ_0 the flux quantum and $E_J = \phi_0 I_c/2\pi$ the Josephson energy. Then, when the qubit energy is $\hbar\omega_q n_q \simeq E_J$, the junction goes to the normal state and we observe the bare cavity frequency.

Appendix F. Raman characterization

Micro-Raman analysis was performed using a laser with a wavelength of 532 nm and a power of approximately 10 mW to avoid laser-induced damage. Photon energy was calibrated using a Si reference via an 1800 lines/mm grating. The beam diameter was around 2 μm to facilitate the measurement on a single flake. The measurement was performed at 300 K on a flake from the same batch of $NbSe_2$ used to fabricate the qubit. We avoided direct investigation of the device to minimize the risk of damaging the JJ. The Raman spectrum is reported in figure 14. The Raman-active modes A_{1g} and E^1_{2g} of the 2 H phase of $NbSe_2$ are clearly observable, confirming the good quality of the material [31].

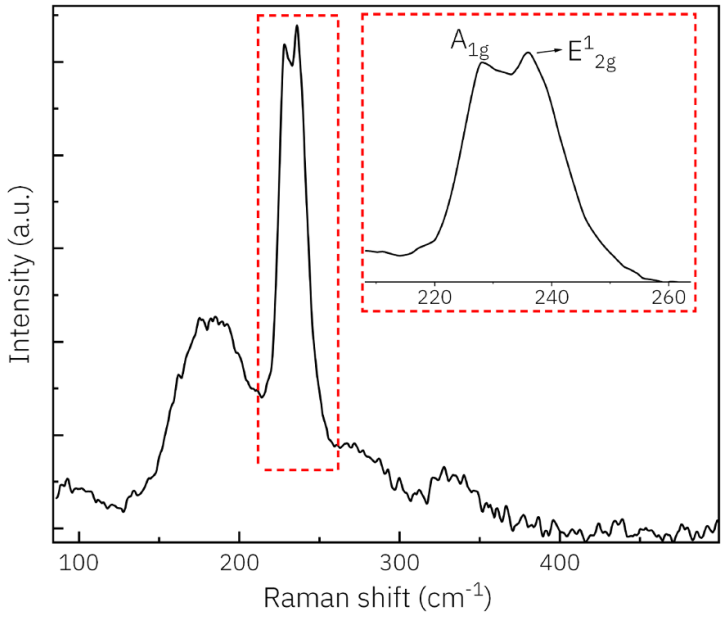


Figure 14. Raman spectrum of a $NbSe_2$ flake.

Appendix G. DC characterization of the $NbSe_2$ junction

To investigate the electrical properties of the native NbO_x barrier formed between the two $NbSe_2$ flakes, we performed DC transport measurements on a test JJ fabricated using the same transfer procedure adopted for the qubit device. In this test structure, the $NbSe_2$ flakes were transferred onto a pre-patterned Si substrate equipped with Pt contacts (see figure 15(a)). At room temperature, the measured junction resistance was approximately 10 kΩ. Such a large resistance is consistent with the presence of a low-transparency barrier between the two overlapping $NbSe_2$ flakes, rather than a direct metallic contact.

The minimum temperature accessible in our DC transport setup is 2.5 K, and therefore a direct resistance measurement at the 20 mK operating temperature of the qubit experiment could not be performed. Upon cooling the test junction below the superconducting transition, however, we observed the onset of a Josephson supercurrent (figures 15(b) and (c)). At 2.5 K, the measured critical current was approximately

$$I_c\,(2.5\ \mathrm{K}) \simeq 60\ \mu\mathrm{A}.$$

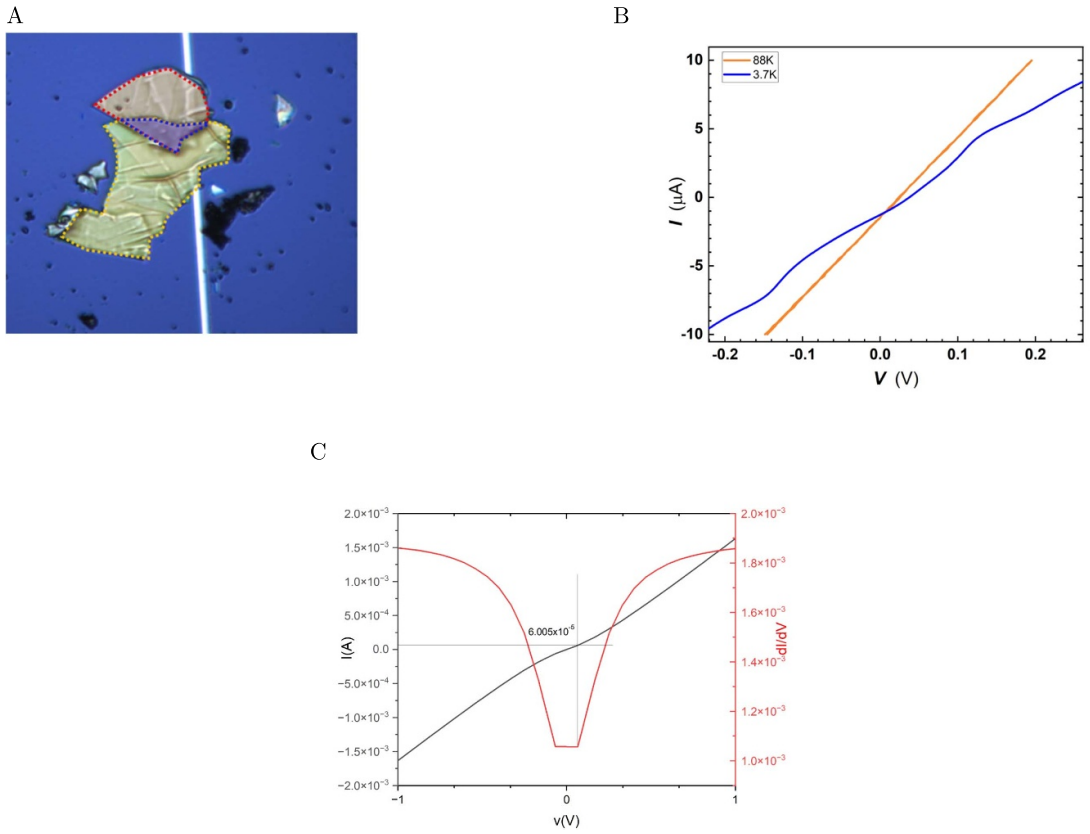


Figure 15. (A) Optical image of the NbS10^2 JJ fabricated for Dc measurements. The JJ area (552 μm^2) is highligted in blue. For reference, the Pt electrode has a width of 4 μ m. (B) *I–V* curves acquired at 88 K and 3.7 K. (C) *I–V* curve at 2.5 K in black and its derivative in red.

Assuming a critical temperature $T_c \simeq 3.7$ K for this device and using the Ambegaokar–Baratoff temperature dependence, we estimate a zero-temperature critical current of approximately

$$I_c\,(20\ \text{mK}) \simeq 90\ \mu\text{A}.$$

This value is approximately a factor of 2.7 smaller than the critical current $I_c = 249\ \mu$A inferred for device Q1)that has the most similar dimensions to the measured JJ) from its spectroscopic parameters. We consider this variation compatible with the reproducibility expected from the present fabrication procedure. Both junctions were assembled under ambient conditions, and neither the thickness nor the microscopic uniformity of the native NbO_x barrier is directly controlled. In addition, variations in the relative orientation and overlap geometry of the two $NbSe_2$ flakes can modify the junction properties.

The combination of a large room-temperature resistance and the emergence of a finite Josephson supercurrent below T_c supports the interpretation of the native NbO_x layer as the weak-link barrier responsible for the Josephson coupling between the two $NbSe_2$ flakes. We emphasize, however, that these measurements were performed on a separate test structure fabricated using the same methodology and do not constitute a direct measurement of the normal-state resistance or critical current of the specific qubit device investigated in the main text.

Improved control over the barrier properties, and consequently over I_c and the qubit transition frequency, will require a more reproducible junction fabrication process. Possible approaches include lithographically defined junction areas combined with a van der Waals insulating barrier of controlled thickness, which would reduce device-to-device variations associated with the uncontrolled formation of the native oxide.

Appendix H. Rabi frequency vs drive amplitude

We studied the evolution of the Rabi frequency (f_{Rabi}) as a function of the drive amplitude (expressed as the square root of the effective cavity occupation number, $\sqrt{n_\gamma}$). The two-dimensional map of the Rabi

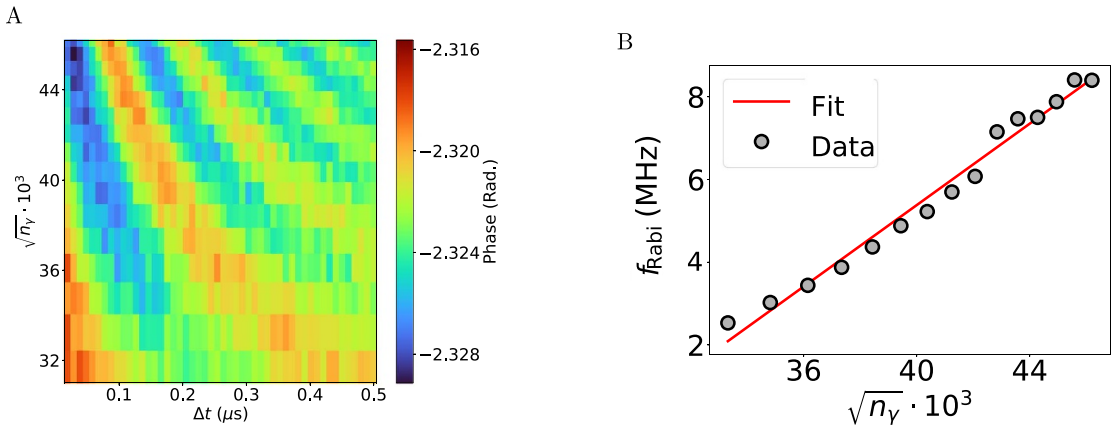


Figure 16. (A) Map of the Rabi oscillations as a function of the drive power. (B) Dependence of the Rabi frequency on the square root of the average occupation number.

oscillations as a function of the excitation pulse duration (Δt) and n_γ is reported in figure 16(a). We set the drive frequency $f_d = f_{01}$. The trend of f_{Rabi} (extracted through a fitting procedure) as a function of $\sqrt{n_\gamma}$ is reported in figure 16(b). The trend is linear, indicating that dynamic is predominantly confined to the $|0\rangle - |1\rangle$ subspace, in agreement with the observed high anharmonicity [27–29].

Appendix I. Rabi frequency vs detuning

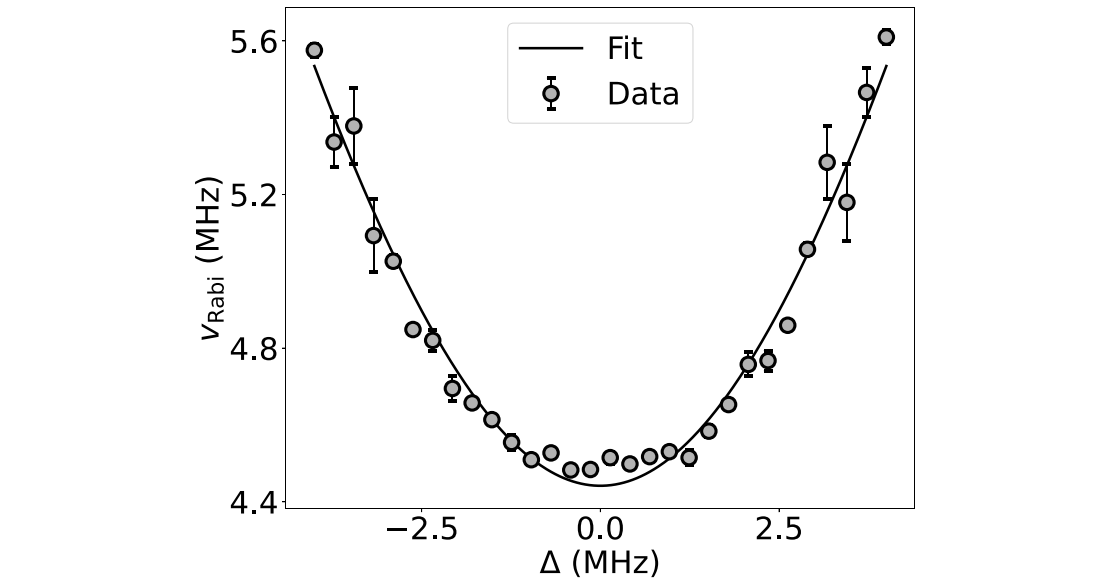


Figure 17. Rabi frequency as a function of the drive detuning from f_{01}.

The evolution of the Rabi frequency can also be studied as a function of the detuning Δ from ω_{01} [32].

$$\omega_{\text{Rabi}}^2 = 4g^2 n_\gamma - \frac{\Gamma^2}{4} + m\Delta^2 . \tag{8}$$

From the Chevron plot reported in figure 3(b) we extracted the dependence of the Rabi frequency on the drive detuning.

The data are reported in figure 17 and fitted using (8). A good fit was obtained by introducing a dimensionless coefficient $m = 0.681$ multiplying Δ^2, indicating the presence of a detuning-dependent dissipation process [33].

References

[1] Laucht A *et al* 2021 Roadmap on quantum nanotechnologies *Nanotechnology* **32** 162003
[2] Becher C *et al* 2023 2023 roadmap for materials for quantum technologies *Mater. Quantum Technol.* **3** 012501
[3] Blais A, Grimsmo A L, Girvin S M and Wallraff A 2021 Circuit quantum electrodynamics *Rev. Mod. Phys.* **93** 025005
[4] Bland M P *et al* 2025 Millisecond lifetimes and coherence times in 2D transmon qubits *Nature* **647** 343–348
[5] Guo G-L, Leng H-B and Liu X 2024 Parity-spin superconducting qubit based on topological insulators *New J. Phys.* **26** 063005
[6] Liu X and Hersam M C 2019 2D materials for quantum information science *Nat. Rev. Mater.* **4** 669–84
[7] Kim H, Jang G, Jin S, Shin D, Shin H-J, Luo J, Siddiqi I, Kim Y, Yoon H H, and Nguyen L B 2025 Josephson junctions in the age of quantum discovery (arXiv:2505.12724)
[8] Wang J I-J *et al* 2019 Coherent control of a hybrid superconducting circuit made with graphene-based van der Waals heterostructures *Nat. Nanotechnol.* **14** 120–5
[9] Di Battista G, Fong K C, Díez-Carlón A, Watanabe K, Taniguchi T and Efetov D K 2024 Infrared single-photon detection with superconducting magic-angle twisted bilayer graphene *Sci. Adv.* **10** ead3725
[10] Nowakowski K *et al* 2025 Single-photon detection enabled by negative differential conductivity in moiré superlattices *Science* **389** 644–9
[11] Walsh E D *et al* 2021 Josephson junction infrared single-photon detector *Science* **372** 409–12
[12] Huang B *et al* 2026 Thermal detection of single photons using Dirac fermions *Nat. Commun.* **17** 3845
[13] Zalic A, Taniguchi T, Watanabe K, Gazit S and Steinberg H 2023 High magnetic field stability in a planar graphene-NbSe2 SQUID *Nano Lett.* **23** 6102–8
[14] Wu H, Wang Y, Xu Y, Sivakumar P K, Pasco C, Filippozzi U, Parkin S S, Zeng Y-J, McQueen T and Ali M N 2022 The field-free josephson diode in a van der waals heterostructure *Nature* **604** 653–6
[15] Bauriedl L *et al* 2022 Supercurrent diode effect and magnetochiral anisotropy in few-layer NbSe2 *Nat. Commun.* **13** 4266
[16] Antony A *et al* 2021 Miniaturizing transmon qubits using van der Waals materials *Nano Lett.* **21** 10122–6
[17] Wang J I *et al* 2022 Hexagonal boron nitride as a low-loss dielectric for superconducting quantum circuits and qubits *Nat. Mater.* **21** 398–403
[18] Brosco V, Serpico G, Vinokur V, Poccia N and Vool U 2024 Superconducting qubit based on twisted cuprate van der Waals heterostructures *Phys. Rev. Lett.* **132** 017003
[19] Sushkov A O 2023 Quantum science and the search for axion dark matter *PRX Quantum* **4** 020101
[20] Kono S, Koshino K, Tabuchi Y, Noguchi A and Nakamura Y 2018 Quantum non-demolition detection of an itinerant microwave photon *Nat. Phys.* **14** 546–9
[21] Dixit A V, Chakram S, He K, Agrawal A, Naik R K, Schuster D I and Chou A 2021 Searching for dark matter with a superconducting qubit *Phys. Rev. Lett.* **126** 141302
[22] Chen S, Fukuda H, Inada T, Moroi T, Nitta T and Sichanugrist T 2024 Search for QCD axion dark matter with transmon qubits and quantum circuit *Phys. Rev. D* **110** 115021
[23] Xi X, Wang Z, Zhao W, Park J-H, Law K T, Berger H, Forró L, Shan J and Mak K F 2016 Ising pairing in superconducting NbSe2 atomic layers *Nat. Phys.* **12** 139–43
[24] Balgley J *et al* 2025 Coherent and compact van der Waals transmon qubits (arXiv:2512.08059)
[25] Yabuki N, Moriya R, Arai M, Sata Y, Morikawa S, Masubuchi S and Machida T 2016 Supercurrent in van der Waals Josephson junction *Nat. Commun.* **7** 10616
[26] Castellanos-Gomez A, Buscema M, Molenaar R, Singh V, Janssen L, Zant H S V D and Steele G A 2014 Deterministic transfer of two-dimensional materials by all-dry viscoelastic stamping *2D Mater.* **1** 011002
[27] Théry A, Neukelmance B, Hue B, Legrand W, Jarjat L, Craquelin J, Villiers M, Cottet A, Delbecq M and Kontos T 2024 Observation of quantum oscillations in the extreme weak anharmonic limit *Phys. Rev. B* **109** 064505
[28] Claudon J, Zazunov A, Hekking F W and Buisson O 2008 Rabi-like oscillations of an anharmonic oscillator: classical versus quantum interpretation *Phys. Rev. B* **78** 184503
[29] Amin M 2006 Rabi oscillations in systems with small anharmonicity *Low Temp. Phys.* **32** 198–204
[30] Jain A, Bharadwaj P, Heeg S, Parzefall M, Taniguchi T, Watanabe K and Novotny L 2018 Minimizing residues and strain in 2D materials transferred from PDMS *Nanotechnology* **29** 265203
[31] Annawati B D *et al* 2025 Polarized Raman spectroscopy of 2HNbSe2 and 1TVSe2 Single Crystals *J. Raman Spectrosc.* (https://doi.org/10.1002/jrs.70004)
[32] Breuer H-P and Petruccione F 2002 *The Theory of Open Quantum Systems* (Oxford University Press)
[33] Bylander J, Gustavsson S, Yan F, Yoshihara F, Harrabi K, Fitch G, Cory D G, Nakamura Y, Tsai J-S and Oliver W D 2011 Noise spectroscopy through dynamical decoupling with a superconducting flux qubit *Nat. Phys.* **7** 565–70